

A 324-Element Vivaldi Antenna Array for Radio Astronomy Instrumentation

Edwin Walter Reid, Laura Ortiz-Balbuena, Aliakbar Ghadiri, *Student Member, IEEE*, and Kambiz Moez, *Member, IEEE*

Abstract—This paper presents a 324-element 2-D broadside array for radio astronomy instrumentation which is sensitive to two mutually orthogonal polarizations. The array is composed of cruciform units consisting of a group of four Vivaldi antennas arranged in a cross-shaped structure. The Vivaldi antenna used in this array exhibits a radiation intensity characteristic with a symmetrical main beam of 87.5° at 3 GHz and 44.2° at 6 GHz. The measured maximum side/backlobe level is 10.3 dB below the main beam level. The array can operate at a high frequency of 5.4 GHz without the formation of grating lobes.

Index Terms—Radio astronomy instrumentation, ultra-wideband (UWB) antenna, Vivaldi antenna.

I. INTRODUCTION

OBSERVATIONAL radio astronomy is concerned with the measurement of electromagnetic radiation emitted by cosmic radio sources, where the radiation is a rapidly and irregularly varying function of time. During the past decade, plans for significantly improving the observing capability in radio astronomy at meter and centimeter wavelengths have received increasingly prominent consideration [1]–[4]. This results from the need for superior sensitivity and high survey speed, required for the study of many astronomical and cosmological phenomena [5]. The instrument used for the measurement of the cosmic radio waves consists of three basic components operating in tandem: a receiving antenna, a sensitive receiver, and a data recorder. The antenna–receiver combination, called a radio telescope, acts like a bolometer in which the antenna’s radiation resistance measures the equivalent temperature of distant parts of the space. This antenna is a critical element in building a sensitive radio astronomy instrument. The objective of this paper is to develop a highly sensitive phased array antenna that is to be used as the feed system for the large adaptive reflector (LAR) radio telescopes [6]. The phased array can be viewed as a way of discretely sampling an aperture, and it must therefore obey

Manuscript received February 10, 2011; revised May 3, 2011; accepted May 5, 2011. Date of publication August 4, 2011; date of current version December 8, 2011. This work was supported by the Natural Sciences and Engineering Research Council of Canada. The Associate Editor coordinating the review process for this paper was Dr. Matteo Pastorino.

E. W. Reid is with Radio Frequency Works, St. Albert, AB T8N 7J1, Canada.

L. Ortiz-Balbuena is with the Universidad Autonoma Metropolitana, Mexico City D.F. C.P. 09340, Mexico.

A. Ghadiri and K. Moez are with the Department of Electrical and Computer Engineering, University of Alberta, Edmonton, AB 26G 2V4, Canada (e-mail: ghadirib@ece.ualberta.ca; kambiz@ece.ualberta.ca).

Color versions of one or more of the figures in this paper are available online at <http://ieeexplore.ieee.org>.

Digital Object Identifier 10.1109/TIM.2011.2159414

the laws of sampling theory over the entire bandwidth. Hence, the array elements must be spaced close enough (less than one wavelength (λ) apart at the shortest wavelength in the receiving band) to avoid undersampling. Undersampling manifests itself as the appearance of grating lobes in addition to the main lobe. On the other hand, placing the array elements very close to each other causes distortion in the received signal because of the mutual coupling of the neighboring array elements [7]. One way of reducing the mutual coupling is to use a large number of low-gain small array elements instead of a few large elements as they exhibit less mutual coupling with each other because of their smaller physical area of influence. Also, the placement of elements over a ground plane tends to reduce the coupling even further because of the canceling effect of the out-of-phase images. A conservative approach is to limit the longest wavelength of the received signal to $\lambda/2$ so that the effect of interelement coupling is small. There are many references supporting the claim that Vivaldi antenna elements can be spaced more closely than $\lambda/2$ apart without suffering excessive mutual coupling at the longest wavelength in the band [8]–[13].

This paper is organized as follows. In Section II, we present the theory on radiation from Vivaldi antennas and provide a closed-form method for computing its radiation pattern. Section III explains the details on the construction of the antenna. In Section IV, we describe the design of the experimental array using modular cruciform units and address the interelement coupling effects. Finally, in Section V, the simulation and measurement results of one Vivaldi antenna element and the entire array are presented.

II. VIVALDI ANTENNA

The Vivaldi antenna has been utilized in many radio frequency (RF) applications such as radio astronomy, ground penetrating radar, ultra-wideband (UWB) communication systems, and UWB imaging system because of its simple structure, light weight, wideband characteristics, low cross polarization, and highly directive patterns [14]–[17]. The Vivaldi antenna consists of an exponentially tapered slot cut in a metal film (with or without a thin substrate) on one side of the material. The narrow slot toward one end is coupled to a transmission line, usually using a balun. Away from this region, the slot is exponentially tapered, and a travelling wave, propagating along the slot, radiates in the end-fire direction. Vivaldi antennas are two to six wavelengths in length, and therefore, they have a very wide pattern bandwidth and high directivity with low sidelobes and

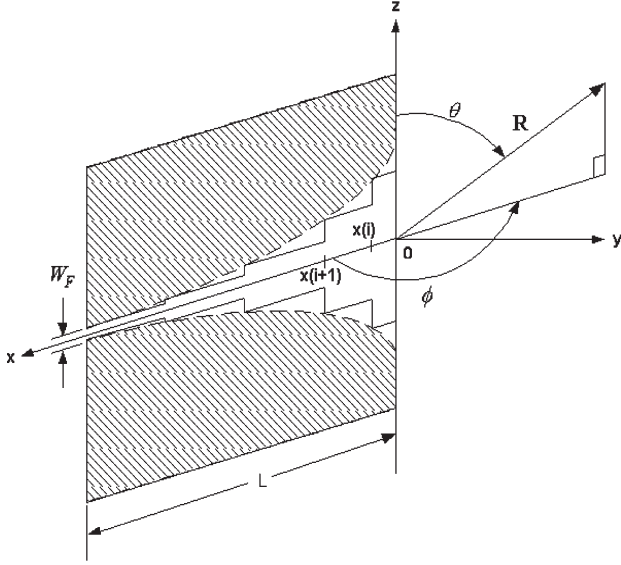


Fig. 1. Stepped approximation of a Vivaldi antenna.

can be designed to produce an axis-symmetrical main beam [8]. They are well suited for microwave frequencies (above 1 GHz) for which a long electrical length yields a practical geometric length, and they can potentially have low dissipative losses. In this section, we develop a theoretical model for the radiation characteristic of a general tapered slot antenna. The theoretical model provides insight on the radiation mechanism of Vivaldi antenna and a method to compute its pattern. A Vivaldi antenna can be constructed from a cascade of interconnected slot-line segments $i = (1, 2, 3, \dots)$ centered along the x -axis with gap width W^i corresponding to the segment i , shown in Fig. 1. The model is based on Itoh's analysis [18]. The transversal aperture field within the slot-line $E_A^i(x, z)$ is given by

$$E_A^i(x, z) = a_1 e^{j\beta_g^i(x-L)} f_1(z) \quad (1)$$

where $\beta_g^i = 2\pi/\lambda_g^i$, λ_g^i is the guide wavelength of the slot-line at segment i , and

$$f_1(z) = \left(\frac{2}{\pi W^i} \right) \frac{1}{\sqrt{1 - \left(\frac{2z}{W^i} \right)^2}} \quad (2)$$

In the derivation of the E - and H -plane radiation patterns, the Fourier transform of $f_1(z)$, denoted as $\tilde{f}_1(\alpha)$, is required, which is

$$\tilde{f}_1(\alpha) = J_0 \left(\frac{\alpha W^i}{2} \right) \quad (3)$$

where α is the transform variable and $J_0(\alpha W^i/2)$ is the Bessel function of the first kind of zero order. Enforcing the conservation of energy principle for power flowing along the entire tapered slot-line results in $a_1 = \sqrt{Z_g^i}$. Therefore

$$\tilde{E}_A^i(x, \alpha) = e^{j\beta_g^i(x-L)} \sqrt{Z_g^i} J_0 \left(\frac{\alpha W^i}{2} \right) \quad (4)$$

The far-field $G(\theta, \phi; x, z)$ is used as the radiation pattern. This field due to an x -directed infinitesimal slot located at (x, z)

on a conducting half-plane is given by [19]

$$G(\theta, \phi; x, z) = |\sin \phi| e^{j\pi/4} F(v) e^{j\beta_0(x \sin \theta \cos \phi + z \cos \theta)} + e^{-j\pi/4} \frac{\sin \left(\frac{\phi}{2} \right) e^{-j\beta_0(x \sin \theta - z \cos \theta)}}{\sqrt{\pi k_0 x \sin \theta}} \quad (5)$$

where $F(v)$ is the complex Fresnel integral [20], β_0 is the freespace wavenumber, and $v = \beta_0 x \sin \theta (1 + \cos \phi)$. The radiation pattern for the i th section of the stepped slot-line approximation is expressed as

$$E_\theta^i(\theta, \phi) = \iint_{\text{Section } i} G(\theta, \phi; x, z) E_{AP}^i(x, z) dx dz \quad (6)$$

By adding up the contributions from all sections of the slot-line, we obtain

$$E_\theta(\theta, \phi) = \sum_{i=1}^N E_\theta^i(\theta, \phi) \quad (7)$$

The E -plane radiation pattern was extracted by specializing the Green's function at $\phi = \pi$. Therefore

$$E_\theta^i(\theta, \pi) = \frac{e^{-j\pi/4}}{\beta_0} \sqrt{Z_g^i} J_0 \left(\frac{\beta_0 W^i \cos \theta}{2} \right) \sqrt{\frac{2}{\sin \theta}} \times \left\{ e^{-j\beta_0 c^i L} \frac{F^*(u_h^i) - F^*(u_l^i)}{\sqrt{c^i - \sin \theta}} + \Gamma e^{j\beta_0 c^i L} \frac{F(\bar{u}_h^i) - F(\bar{u}_l^i)}{\sqrt{c^i + \sin \theta}} \right\} \quad (8)$$

where $u_l^i = \beta_0(c^i - \sin \theta)x_l^i$, $\bar{u}_l^i = \beta_0(c^i + \sin \theta)x_l^i$, $u_h^i = \beta_0(c^i - \sin \theta)x_h^i$, $\bar{u}_h^i = \beta_0(c^i + \sin \theta)x_h^i$, $c^i = \lambda_0/\lambda_g^i$, and Γ is the reflection coefficient due to a backward travelling wave on the aperture. Now, the H -plane radiation pattern is obtained by specializing the Green's function at $\theta = \pi/2$. Thus

$$E_\theta^i \left(\frac{\pi}{2}, \phi \right) = \frac{e^{-j\pi/4}}{\beta_0} e^{-j\beta_0 c^i L} \sqrt{Z_g^i} \times \left\{ \frac{|\sin \phi|}{(c^i + \cos \phi)} \cdot [F(p_h^i) e^{jv_h^i} - F(p_l^i) e^{jv_l^i}] - \frac{|\sin \phi|}{(c^i + \cos \phi)} \cdot \sqrt{\frac{1 + \cos \phi}{(c^i - 1)}} [F^*(q_h^i) - F^*(q_l^i)] + \sin \left(\frac{\phi}{2} \right) \sqrt{\frac{2}{c^i - 1}} [F^*(q_h^i) - F^*(q_l^i)] \right\} + \Gamma \frac{e^{-j\pi/4}}{\beta_0} e^{j\beta_0 c^i L} \sqrt{Z_g^i} \times \left\{ \frac{|\sin \phi|}{(c^i - \cos \phi)} \cdot [F(p_h^i) e^{-j\bar{v}_h^i} - F(p_l^i) e^{-j\bar{v}_l^i}] - \frac{|\sin \phi|}{(c^i - \cos \phi)} \cdot \sqrt{\frac{1 + \cos \phi}{(c^i + 1)}} [F(\bar{q}_h^i) - F(\bar{q}_l^i)] - \sin \left(\frac{\phi}{2} \right) \sqrt{\frac{2}{c^i + 1}} [F^*(\bar{q}_h^i) - F^*(\bar{q}_l^i)] \right\} \quad (9)$$

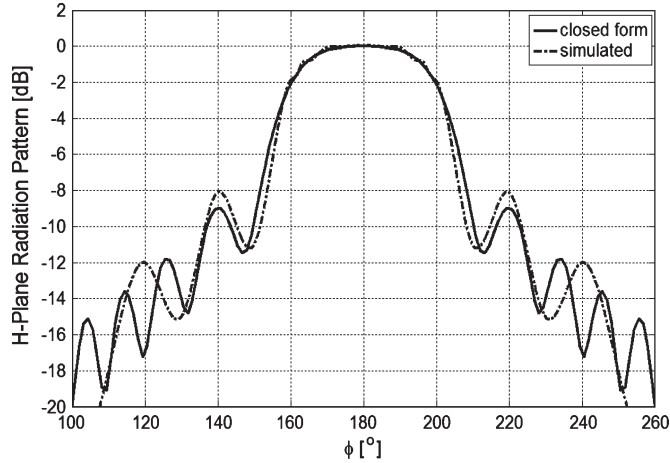

 Fig. 2. Closed-form versus simulated H -plane radiation patterns.

TABLE I

COMPARISON OF THE CALCULATION AND SIMULATION RESULTS FOR THE SALIENT FEATURES OF THE E - AND H -PLANE RADIATION PATTERNS. THE ABBREVIATIONS BW, SLL, AND BWFN STAND FOR BEAMWIDTH, SIDELOBE LEVEL, AND BEAMWIDTH FIRST NULLS, RESPECTIVELY

Parameters	E-plane		H-plane	
	Cal.	Sim.	Cal.	Sim.
3-dB BW	36°	38°	45°	42°
10-dB BW	50°	55°	60°	55°
1st SLL	-8.4 dBi	-8.5 dBi	-9 dBi	-8 dBi
2nd SLL	-11.2 dBi	-11 dBi	-12 dBi	-12 dBi
BWFN	72°	80°	63°	60°
BW 1st SL	86°	92°	80°	80°

where $\bar{v}_h^i = \beta_0(c^i - \cos \phi)x_h^i$, $\bar{v}_l^i = \beta_0(c^i - \cos \phi)x_l^i$, $\bar{q}_h^i = \beta_0(c^i + 1)x_h^i$, and $\bar{q}_l^i = \beta_0(c^i + 1)x_l^i$.

Finally, to obtain the far-field radiation, for a 45° cut, we can set $\theta = \phi$ in (5), and then, we can evaluate (6) and (7) [21]. These developed closed-form equations provide an expedient computation of radiation patterns, which allows the designer to determine an initial set of antenna dimensions that will reduce the number of simulation iterations. Using the aforementioned closed-form equations and approximating the exponentially tapered slot with three or four segmented slot-lines (as shown in Fig. 1), the designer can find the initial antenna dimensions for the desired radiation pattern (e.g., 45°) at the defined center frequency (4.5 GHz in this paper). The initial design is simulated using the 3-D electromagnetic simulation tool (CST Microwave Studio) to evaluate the performance characteristics of the antenna, such as the radiation pattern. Finally, the Vivaldi antenna dimensions are optimized using the simulation tool to achieve the desired radiation pattern at the defined frequency band. As an example, Fig. 2 shows the H -plane radiation power pattern of a Vivaldi element whose element length and aperture are optimized to 4λ and λ to achieve a radiation pattern of 45° at the frequency band of 3–6 GHz. Table I compares the calculation (using the closed-form equations) and simulation results for the salient features of the E - and H -plane radiation patterns. The abbreviations BW, SLL, and BWFN stand for beamwidth, sidelobe level, and beamwidth first nulls, respectively. The example shows that the E - and H -plane radiation

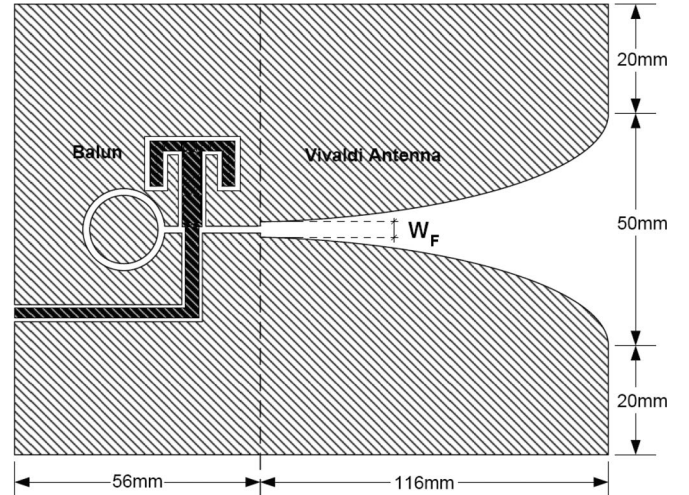


Fig. 3. Detailed drawing of the experimental Vivaldi antenna.

patterns computed using (8) and (9) provide agreement to the simulation within 10% discrepancy.

III. VIVALDI ANTENNA DESIGN

The initial antenna dimensions were obtained using the aforementioned closed-form equations to get an expedient first approximation. This was followed by simulation using CST Microwave Studio to optimize the design and to obtain the final dimensions. The simulation results present important information on antennas, such as surface current on conductors and total radiated power, which could not otherwise be found through analytical methods. The experimental antenna was constructed from Rogers Duroid RT/5880 RF printed circuit board material. The dielectric material and copper thicknesses are 800 and $250 \mu\text{m}$, respectively. Fig. 3 shows the dimensions of the Vivaldi antenna. The gap width on the left side of the Vivaldi antenna, denoted by W_F , is called as feed-gap. The circular object and the vertical “T”-shaped object at the left of the dotted line are the antenna’s balun.

In the same figure, the curves are determined by the expression

$$z(x) = \pm \frac{W}{2} e^{-px}, \quad 0 \leq x \leq L \text{ where } p = -\frac{1}{L} \ln \left(\frac{W_F}{W} \right). \quad (10)$$

As shown in Fig. 4, we used a planar fourth-order Marchand balun [22], [23] which consists of a resonator, a compensator, a cross-junction, and two quarter-wavelength impedance transformers. Design equations are taken from [23], with some modifications to accommodate our implementation. The resonator consists of two semicircular series-connected quarter-wavelength slot-line sections, joined at the ends, which is normally terminated with a short circuiting bar. Since the lines are connected in series at the cross-junction, the electric field vector in one line lies in an opposite direction to the other. Now, at a distance $\lambda_g/4$ from the cross-junction, the net electric fields will sum up to zero. This is equivalent to terminating the individual lines with short circuits, producing a virtual

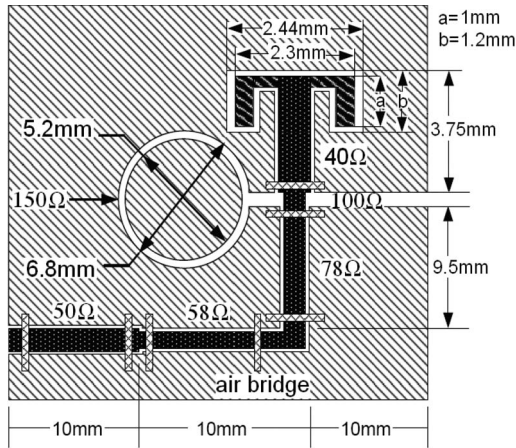


Fig. 4. Marchand balun.

short circuit. The compensator is a quarter-wave open-circuit stub, constructed from coplanar waveguide (CPW). One of the quarter-wave transformers is a CPW, and the other is a slot-line. At the center of the operating band, the resonator appears as an open circuit at the cross-junction, while the compensator appears as a short circuit. In Fig. 4, the shaded regions are $25\text{-}\mu\text{m}$ -thick copper surfaces printed on a 0.8-mm -thick RT/5880 dielectric. All CPW and slot-line gaps are 0.3 mm wide. Trace widths are 2.5 , 2.0 , 1.0 , and 0.6 mm for the 40- , 50- , 58- , and $78\text{-}\Omega$ CPW sections, respectively. All gaps that flank CPW are 0.3 mm wide. Slot-line gaps are 0.3 and 0.8 mm for the 100- and $150\text{-}\Omega$ slot-line sections, respectively. An end launch SMA jack can be attached to the $50\text{-}\Omega$ CPW appearing at the bottom left-hand side. A Vivaldi antenna is attached to the $100\text{-}\Omega$ slot-line at the right-hand side. An $800\text{-}\mu\text{m}$ -thick $4\text{ mm} \times 8\text{ mm}$ rectangular slab of superstrate (not shown in Fig. 4) with dielectric is bonded to the $40\text{-}\Omega$ CPW compensator.

As shown in Fig. 4, there are seven air bridges to force the CPW to propagate only in odd order modes, particularly in the lowest order mode. The bridges are used to avoid high return loss and, hence, poor transmission of energy to/from the antenna. Air bridges are short copper ribbons about 0.5 mm wide that pass over the center conductor of the CPW electrically connecting the ground planes. This keeps both sides of the CPW ground plane at a common potential, which ensures that only the odd CPW modes will propagate. Air bridges were placed by trial-and-error method. These were soldered to the ground plane at locations which would increase the magnitude of the reflection coefficient. It should be noted that right-angle coplanar transmission-line bends should be mitered or rounded to reduce the effect of excess capacitance. The antenna dimensions are determined by the specification of the lower (f_L) and upper (f_U) passband frequencies over which the balun must operate, where the return loss exceeds a given minimum value based on the design procedure explained in [24].

IV. VIVALDI ANTENNA ARRAY

The array is constructed using a modular design with cruciform units shown in Fig. 5. A cruciform unit consists of four Vivaldi elements arranged in a close-packed group to form

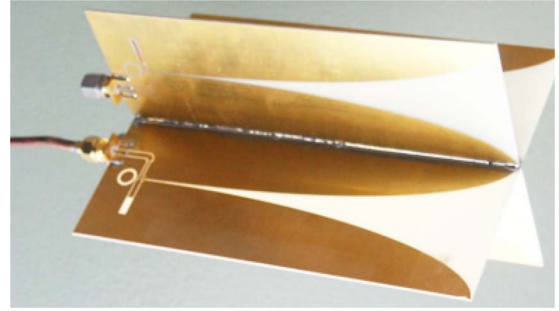


Fig. 5. Cruciform unit.

an electromagnetic element that is sensitive to two mutually orthogonal polarizations. The width of the cruciform unit is a very critical dimension. This is because these units are held in their place on the array by the frictional force at the gap region of the supporting posts. In order to have the array rotatable on a turntable for measuring its radiation pattern, it is important that the array is rigid. This requirement was met by having a backplane in which the posts are inserted with interference fit. A phenomenon known as mutual coupling [25] is creating the exchange of the electromagnetic energy between neighboring antennas in an array, altering the current distribution on antennas that are in close proximity. This effect alters both the antenna's terminal impedance and the radiation pattern of an array from that where there is no coupling. There are three mechanisms responsible for the mutual coupling: 1) the direct space coupling between array elements; 2) the indirect coupling caused by the scattering from nearby objects; and 3) the feed network to interconnect elements in the array. A measure of the strength of mutual coupling between array elements m and n is given by the scattering parameter. Specifically, we are interested in $|s_{mn}|^2$, in which the other elements are assumed to be terminated by matched loads.

V. RESULTS

A. Vivaldi Antenna

An experimental antenna was constructed with the following dimensions: $L = 116\text{ mm}$ for length, $W = 50\text{ mm}$ for aperture, and $W_F = 1\text{ mm}$ for the feed-gap. $\lambda_{des} = c/f_{des}$ is the freespace wavelength at the center frequency, computed as the arithmetic mean of the operating frequency range $3\text{--}6\text{ GHz}$. Thus, $f_{des} = 4.5\text{ GHz}$, and $c = 3 \times 10^8\text{ m/s}$ is the speed of light. Fig. 6 shows the difference between reflection coefficients predicted by simulation and obtained by measurement. Over the frequency range of $3\text{--}6\text{ GHz}$, the envelope of the measured reflection coefficient is $3\text{--}5\text{ dB}$ less than that of the simulated antenna. This result demonstrates that the experimental antenna satisfies the reflection coefficient criteria. The discrepancy between the simulated and measured data is mainly due to the propagation of higher order modes on the antenna.

The experimental Vivaldi antenna was tested using an anechoic chamber. At the center of the chamber sat a turntable which is used to rotate the antenna under test in the horizontal plane. The second antenna was located 4 m away. The control room was equipped with a vector network analyzer (VNA),

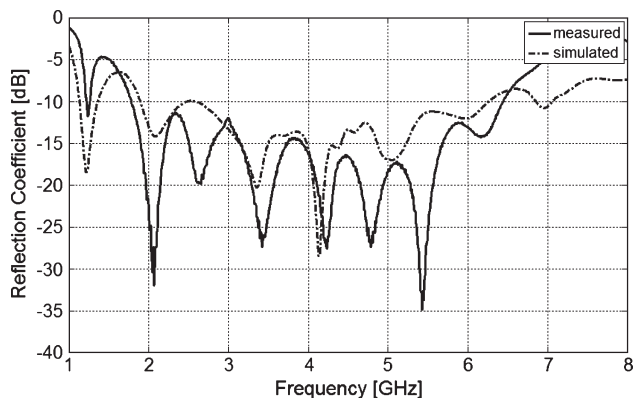


Fig. 6. Measured and simulated reflection coefficients of the Vivaldi antenna.

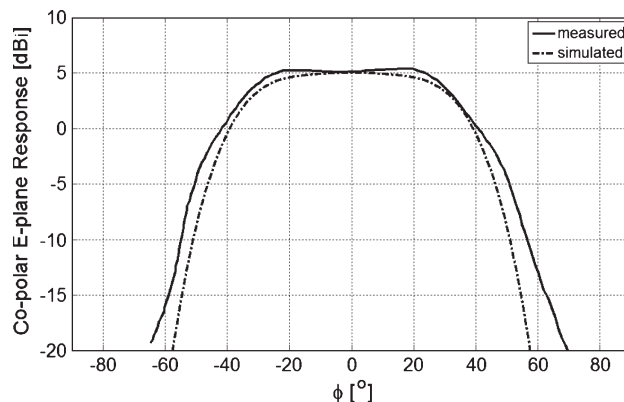


Fig. 9. Measured and simulated copolar *H*-plane responses at 3 GHz.

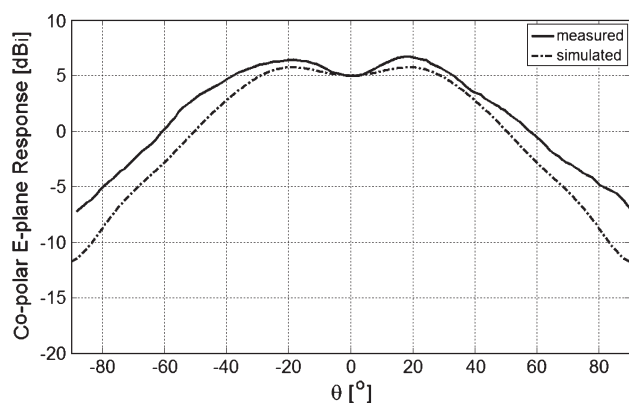


Fig. 7. Measured and simulated copolar *E*-plane responses at 3 GHz.

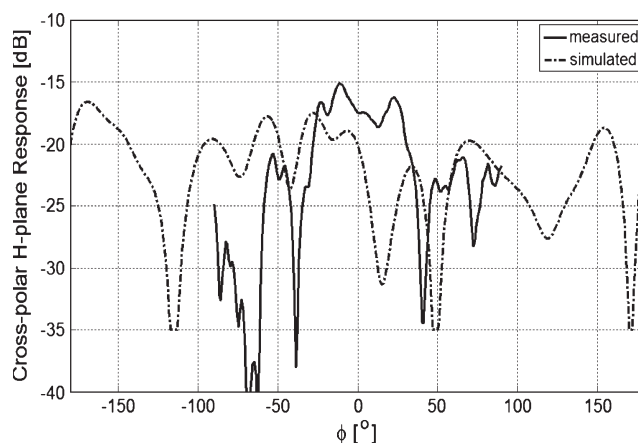


Fig. 10. Measured and simulated cross-polar *H*-plane responses at 3 GHz.

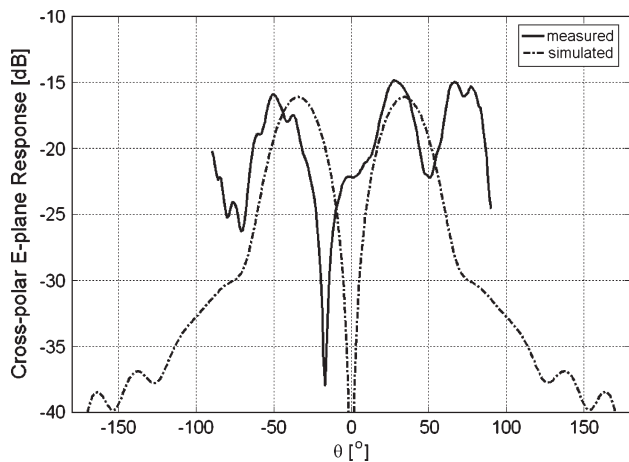


Fig. 8. Measured and simulated cross-polar *E*-plane responses at 3 GHz.

computer, data acquisition system, and turntable controller. A calibration standard horn antenna with known radiation pattern is used to identify regions of significant reflection in the anechoic chamber. Two error sources were identified as the vibration of the structure because of the external sources as the antenna was rotated and the weak VNA output signal of the transmitter port. The second source of error was addressed by using an RF power amplifier to boost the power fed to the antenna. The experimental and simulation results for the antenna are measured at 3 GHz and over the elevation range

of -90° – 90° . Fig. 7 shows the *E*-plane copolar response. The 3-dB beamwidth pattern is 10% wider than the value predicted by simulation. Also, a 3-dB dimple appears on the boresight of both patterns because of the following two reasons: first, the dimple could be caused by currents induced on the upper and lower edges of the element, or second, it could be due to the propagation of higher order modes along the tapered slot in which these currents are out of phase to the primary mode. Fig. 8 shows the measurement and simulation results for the cross-polar response in the *E*-plane. Both responses are 15 dB below the maximum level of the main beam. The difference in the position of sharp null in the cross-polar measurement is due to the error introduced by vibration. Fig. 9 shows the copolar *H*-plane response at 3 GHz. The measured 3-dB beamwidth pattern is 77° . First sidelobes appear at $\pm 90^{\circ}$, which are 9 dB below the level on the boresight. The measured pattern is 10% wider than that predicted by simulation. Also, the response of the measured pattern is more than 20 dB. This is because of the same reasons mentioned for the *E*-plane pattern. Fig. 10 shows the cross-polar response in the *H*-plane. Both responses are 15 dB below the maximum level of the main beam. For sharp null responses, the antenna works very well for polarimetry applications. Fig. 11 shows the measurement and simulation responses on a 45° cut at 3 GHz. We note that there are no beams present in the direction along a diagonal cut.

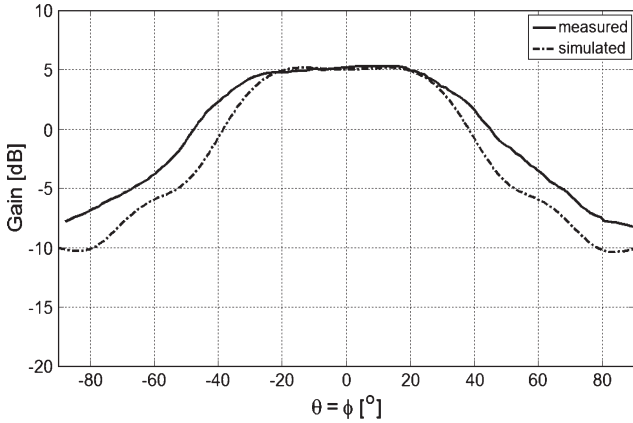


Fig. 11. Measured and simulated responses on a 45° cut at 3 GHz.

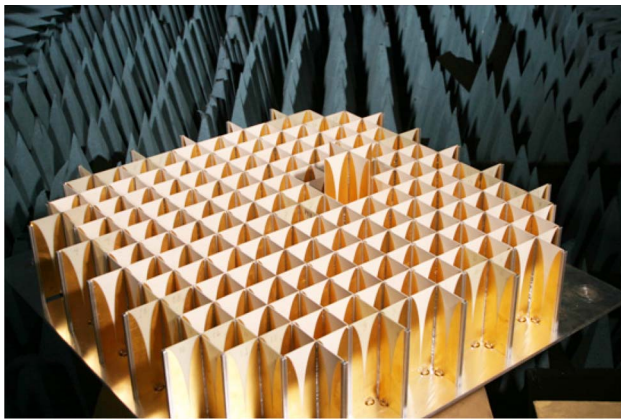


Fig. 12. Front and side views of the proposed array.

B. Vivaldi Antenna Array

The array was constructed in an egg-crate structure, forming a 324-element 2-D broadside, which is sensitive in two mutually orthogonal polarizations. Fig. 12 shows the array structure of closely packed elements. A cruciform unit is lifted out of its place, demonstrating that the units are easily replaced. The frequency range over which the array can operate is provided by the reflection coefficient measurement. This was performed on the individual elements within the array, one at a time, with all other elements terminated with 50-Ω loads. An Agilent model 8720SE VNA was used to measure the reflection coefficients covering the frequency range of 1–8 GHz with 801 frequency samples. This range was used because it exceeds the frequency range over which the elements were expected to radiate effectively. Sample averaging was used to reduce the effects of noise and random errors introduced in the measurements.

In this paper, the criterion that is used to determine the effectiveness of the antenna is that its reflection coefficients should not be more than -10 dB. In order to avoid the possibility that signals generated by the VNA might be reflected by nearby objects and returned to the array, return loss measurements were performed outdoor in a location far away from large objects. All measurements were made with the array pointed at the sky. Fig. 13 shows the reflection coefficient for a typical antenna

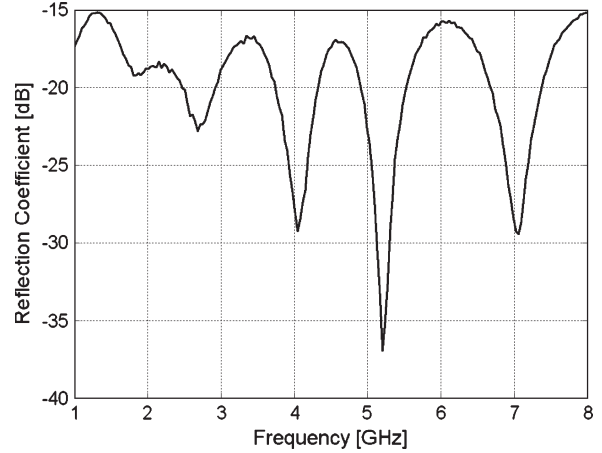


Fig. 13. Measured reflection coefficient for a typical antenna element embedded in the array.

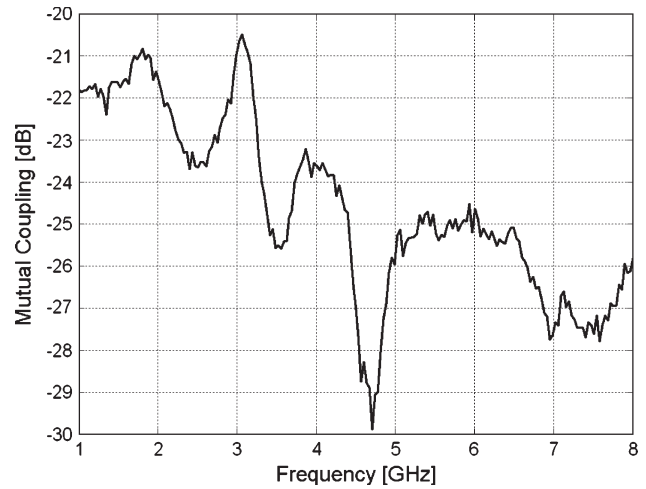


Fig. 14. Measured mutual coupling between the copolar closest elements.

element within the array. The -10-dB reflection coefficient frequency range is 1.8–6.6 GHz, which suggests that the array can be efficiently operated over the same range. Using the same VNA, the mutual coupling between pairs of array elements was measured over the frequency range of 1–8 GHz. Fig. 14 shows the magnitude of mutual coupling (i.e., transmission coefficient in decibels) between the copolar closest elements (the closest neighbors) as a function of frequency. As shown in this figure, the interelement mutual coupling becomes significantly weaker with the increase in the distance between elements. The rapidly fluctuating values of $|s_{mn}|$ is a function of frequency. The general trend is that the coupling decreases as the frequency increases, and this is common for all other element pairs in the array. Fig. 15 shows another sample result in which the mutual coupling takes place between the closest stacked elements, verifying that the coupling decreases with frequency.

The active element pattern $g_{ae}(\theta, \phi)$ was measured using a Scientific Atlanta (MI Technologies) series 5704 virtual vertex compact antenna testing system. The range consists of an indoor anechoic chamber (15 ft high, 20 ft wide, and 36 ft long) along with a parabolic reflector (133 in high and 186 in wide,

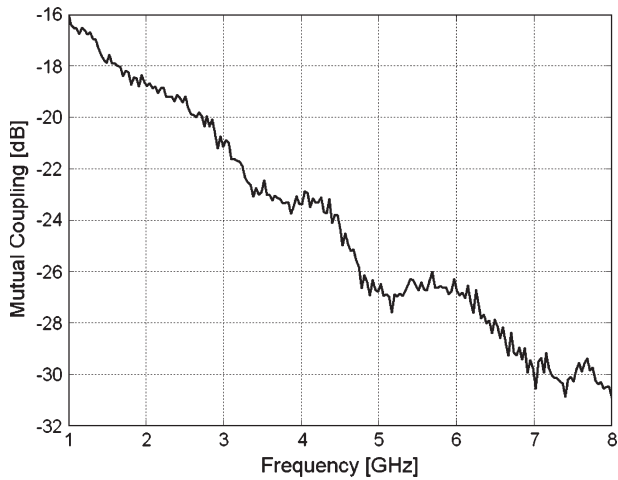


Fig. 15. Measured mutual coupling between the closest stacked elements.

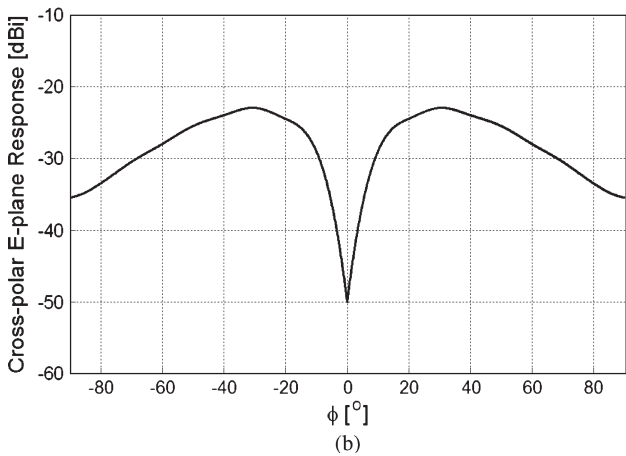
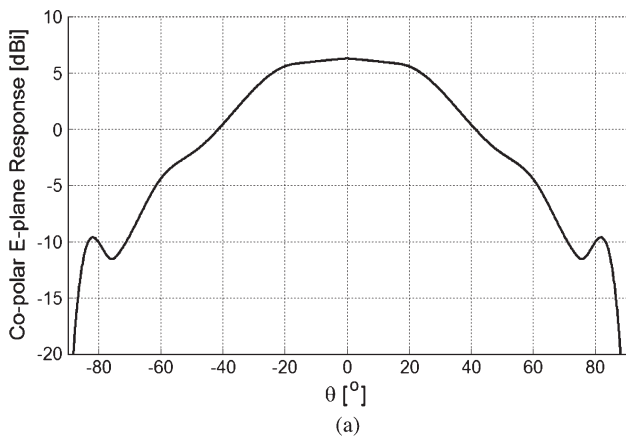


Fig. 16. Measured (a) copolar and (b) cross-polar *E*-plane radiation patterns of the elements close to the center at 3 GHz.

with its vertex fixed to one wall). A feed antenna produces a spherical wave front, and the reflector converts it to a plane wave. The reflector creates a test zone, which accurately simulates the far-field conditions for the antenna or array under test.

The radiation patterns of the elements located close to the center and those on the periphery of the array are measured. Figs. 16(a)–(b) and 17(a)–(b) show the measured copolar

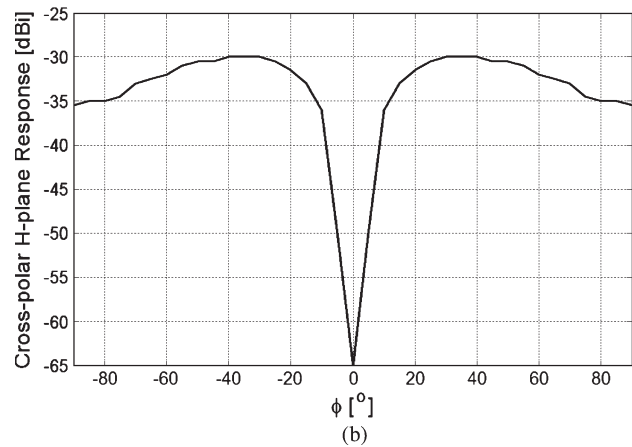
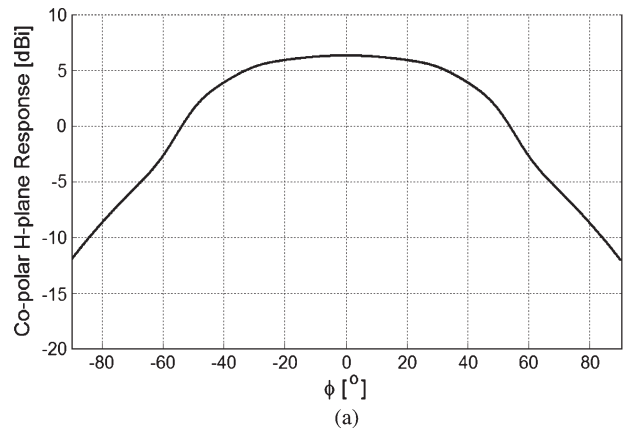


Fig. 17. Measured (a) copolar and (b) cross-polar *H*-plane radiation patterns of the elements close to the center patterns at 3 GHz.

E-plane, cross-polar *E*-plane, copolar *H*-plane, and cross-polar *H*-plane radiation patterns of the elements close to the center at 3 GHz, respectively. The distortion that appears in the copolar radiation patterns is due to the reflections from the mounting hardware and slight bending of the antenna as it was rotated to take the measurements. In the *E*-plane, the 3-dB beamwidth is 58°, and the maximum sidelobe is 17 dB below the peak of the main beam. In the *H*-plane, the 3-dB beamwidth is 90°, and there are no significant sidelobes. Obviously, the main beam is not axisymmetric; however, that does not make the feed unsuitable for a parabolic reflector antenna. An analytical expression was developed in [26] to calculate the polarization discrimination of a parabolic antenna feed at its focal point with a feed antenna, such as a Vivaldi element, which has a certain inherent measure of asymmetry in its *E*- and *H*-plane radiation patterns. It was demonstrated in [26] that, when the ratio of the focal point to the diameter (F/D) is large, the cross polarization discrimination is significantly improved in spite of the fact that a feed with asymmetric *E*- and *H*-plane radiation patterns is used. For the radio telescope application in this paper, the F/D ratio is indeed large (≈ 3). Therefore, we can still use feeds with certain pattern asymmetry. The radiation pattern of the elements located on the periphery of the array differs slightly from those that are embedded. The difference is that the main beam is squinted from the boresight. This squint is caused by array truncation, and its effect is

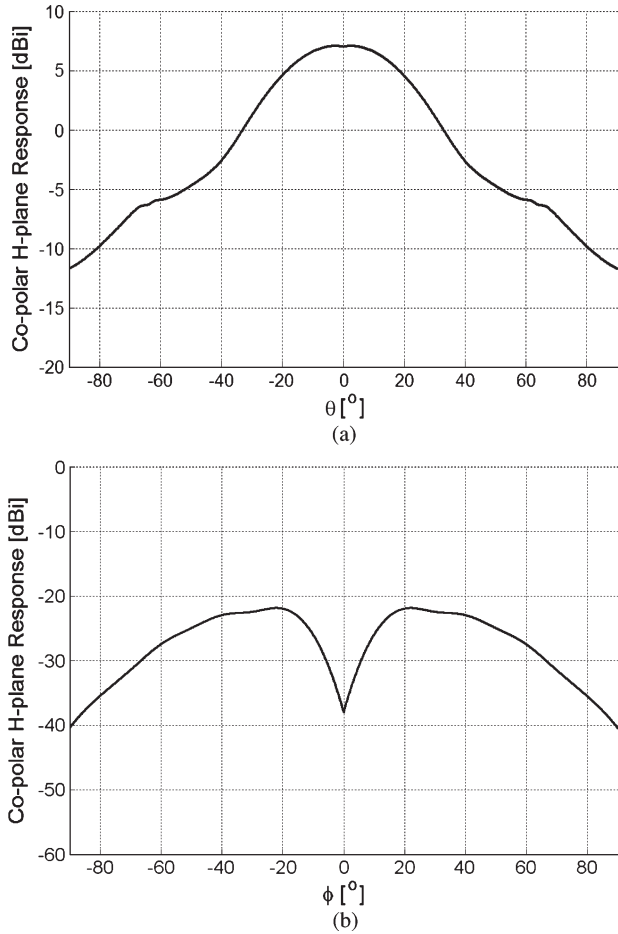


Fig. 18. Measured (a) copolar and (b) cross-polar E -plane radiation patterns of the elements close to the center patterns at 6 GHz.

prominent for the outer elements. The radiation patterns of the elements located close to the center and those on the periphery of the array are measured. As the frequency increases, the E - and H -plane radiation patterns become more symmetric. Figs. 18(a)–(b) and 19(a)–(b) show the measured copolar E -plane, cross-polar E -plane, copolar H -plane, and cross-polar H -plane radiation patterns at 6 GHz, respectively. In the E -plane, the 3-dB beamwidth is 40° , and the maximum side-lobe is 13.5 dB below the peak of the main beam. In the H -plane, the 3-dB beamwidth is 50° , and the maximum side-lobe is 21.4 dB below the peak of the main beam.

Finally, Fig. 20 shows the far-field radiation, in which only four elements were excited with equal current, producing an end-fire main beam with symmetrical E - and H -plane patterns. We found out that the squint for the outer element is more pronounced at the long wavelength (lower frequency) than the short wavelength. This is because, at long wavelengths, the element appears electrically small, which is a condition that results in an asymmetrical current distribution. That is why the peripheral (outer) elements not used should be terminated with matched resistive loads to absorb any parasitic reflection. As seen in the simulation of radiation patterns, the neighboring elements interact with each other, which results in the formation of an axisymmetric beam. The Vivaldi array is established on an instrument platform which is kept afloat by an aerostat

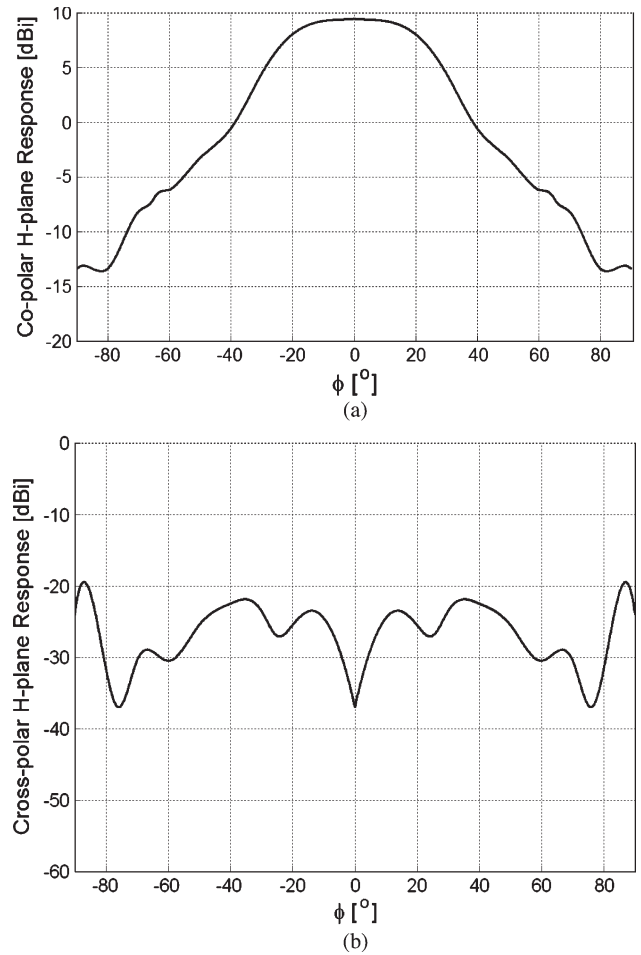


Fig. 19. Measured (a) copolar and (b) cross-polar H -plane radiation patterns of the elements close to the center patterns at 6 GHz.

(fancy name for a helium-filled large balloon) that is stabilized by Kevlar ropes. The 200-m parabolic reflector lies with its vertex on the ground, with the aperture facing the Vivaldi feed array. The Vivaldi feed array is 600 m above ground level and is kept at the focal point by tensioning the Kevlar cables. In addition to the cables, the instrument platform can make fine adjustments in position to maintain focus through the use of a closed-loop feedback control system. It should be reinforced that several beams can be created. This will allow simultaneous observations of the sky. The number of beams depends on the choice of individual beamwidths, which is a function of the beam-forming network, and downstream signal processing.

VI. CONCLUSION

In this paper, we have presented a brief theoretical overview, design, simulation, construction, and measurement on an experimental Vivaldi antenna array. This highly sensitive phased array is used as the feed system for the LAR radio telescopes. The array is composed of cruciform units consisting of four Vivaldi antennas arranged in a cross-shaped structure. The Vivaldi antenna used in this array exhibits a radiation intensity characteristic with a symmetrical main beam of 87.5° at 3 GHz. Also, the mutual coupling between the nearest neighbor

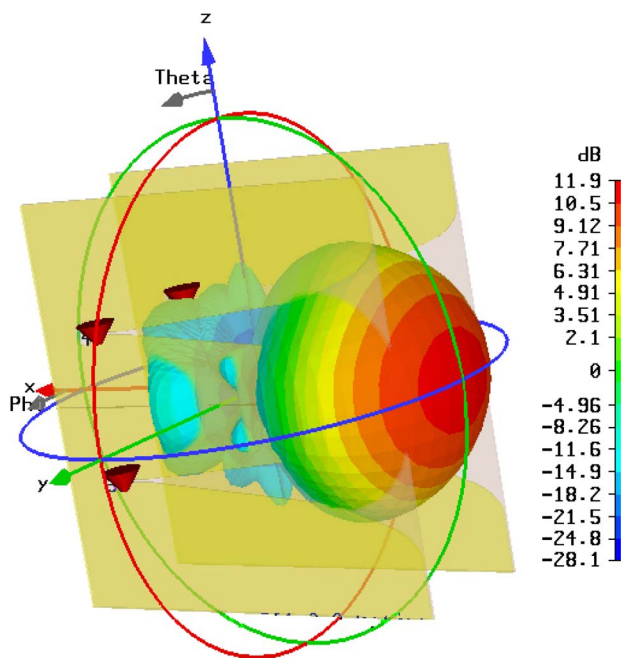


Fig. 20. Far-field radiation pattern.

elements is very weak. The measured maximum side/backlobe level is 10.3 dB below the main beam level. The array can operate at a high frequency of 5.4 GHz without the formation of grating lobes.

REFERENCES

[1] S. Padin, T. Clark, M. Ewing, R. Finch, R. Lawrence, J. Navarro, S. Scott, N. Scoville, C. Seelinger, and T. Seling, "A high-speed digital correlator for radio astronomy," *IEEE Trans. Instrum. Meas.*, vol. 42, no. 4, pp. 793–798, Aug. 1993.

[2] O. Koistinen, J. Lahtinen, and M. T. Hallikainen, "Comparison of analog continuum correlators for remote sensing and radio astronomy," *IEEE Trans. Instrum. Meas.*, vol. 51, no. 2, pp. 227–234, Apr. 2002.

[3] J. Nanbo and Y. Rahmat-Samii, "Analysis and particle swarm optimization of correlator antenna arrays for radio astronomy applications," *IEEE Trans. Antennas Propag.*, vol. 56, no. 5, pp. 1269–1279, May 2008.

[4] I. Malo-Gómez, J. D. Gallego-Puyol, C. Diez-González, I. López-Fernández, and C. Briso-Rodríguez, "Cryogenic hybrid coupler for ultra-low-noise radio astronomy balanced amplifiers," *IEEE Trans. Microw. Theory Tech.*, vol. 57, no. 12, pp. 3239–3245, Dec. 2009.

[5] J. W. M. Baars, L. R. D'Addario, and A. R. Thompson, "Radio astronomy in the early twenty-first century," *Proc. IEEE*, vol. 97, no. 8, pp. 1377–1381, Aug. 2009.

[6] T. H. Legg, "A proposed large radio telescope of new design," *Astron. Astrophys. Suppl.*, vol. 130, pp. 369–379, 1998.

[7] J. D. Kraus, *Antennas*, 3rd ed. New York: McGraw-Hill, 2002.

[8] P. J. Gibson, "The Vivaldi aerial," in *Proc. 9th Eur. Microw. Conf.*, 1979, pp. 101–105.

[9] E. Gazit, "Improved design of the Vivaldi antenna," *Proc. Inst. Elect. Eng.—Microw., Antennas Propag.*, vol. 135, no. 2, pp. 89–92, Apr. 1988.

[10] P. Knott and A. Bell, "Coaxially-fed tapered slot antenna," *Electron. Lett.*, vol. 37, no. 18, pp. 1103–1104, Aug. 2001.

[11] J. Shin and D. H. Schaubert, "A parameter study of stripline-fed Vivaldi notch-antenna arrays," *IEEE Trans. Antennas Propag.*, vol. 47, no. 5, pp. 879–886, May 1999.

[12] K. S. Yngvesson, T. L. Korzeniowski, Y.-S. Kim, E. L. Kollberg, and J. F. Johansson, "The tapered slot antenna—A new integrated element for millimeter-wave applications," *IEEE Trans. Microw. Theory Tech.*, vol. 37, no. 2, pp. 365–374, Feb. 1989.

[13] H. Holter, T.-H. Chio, and D. H. Schaubert, "Experimental results of 144-element dual-polarized endfire tapered-slot phased arrays," *IEEE Trans. Antennas Propag.*, vol. 48, no. 11, pp. 1707–1718, Nov. 2000.

[14] M. Arts, R. Maaskant, E. de Lera Acedo, and J. G. Bij de Vaate, "Broadband differentially-fed tapered slot antenna array for radio astronomy applications," in *Proc. 3rd Eur. Conf. Antennas Propag.*, Mar. 2009, pp. 566–570.

[15] D. Glynn, R. Nesti, J. G. Bij de Vaate, N. Roddis, and E. Limiti, "Realization of a focal plane array receiver system for radio astronomy applications," in *Proc. 39th Eur. Microw. Conf.*, Oct. 2009, pp. 922–925.

[16] M. Chiappe and G. L. Gragnani, "Vivaldi antennas for microwave imaging: Theoretical analysis and design considerations," *IEEE Trans. Instrum. Meas.*, vol. 55, no. 6, pp. 1885–1891, Dec. 2006.

[17] P. Cerný, J. Nevrlý, and M. Mazánek, "Optimization of tapered slot Vivaldi antenna for UWB application," in *Proc. 19th Int. Conf. Appl. Electromagn. Commun.*, Sep. 2007, pp. 1–4.

[18] T. Itoh, *Numerical Techniques for Microwave and Millimeter-Wave Passive Structures*. New York: Wiley, 1989.

[19] C.-T. Tai, *Dyadic Green's Functions in Electromagnetic Theory*. Piscataway, NJ: IEEE Press, 1994, ser. IEEE Oxford University Press Series on Electromagnetic Wave Theory.

[20] J. Boersma, "On a numerical method for the computation of Fresnel integrals," Math. Inst., Univ. Groningen, Groningen, The Netherlands, Rep. TW 2, 1960.

[21] P. R. Acharya, H. Ekstrom, S. S. Gearhart, J. F. Johansson, S. Jacobson, G. M. Rebeiz, and E. L. Kollberg, "Tapered slotline antennas at 802 GHz," *IEEE Trans. Microw. Theory Tech.*, vol. 41, no. 10, pp. 1715–1719, Oct. 1993.

[22] N. Marcband, "Transmission-line conversion transformers," *Electronics*, vol. 17, no. 12, pp. 142–145, Dec. 1944.

[23] V. Trifunovi and B. Jokanovi, "Review of printed Marchand and double Y baluns: Characteristics and application," *IEEE Trans. Microw. Theory Tech.*, vol. 42, no. 8, pp. 1454–1462, Aug. 1994.

[24] S. B. Cohn, "Slot line on a dielectric substrate," *IEEE Trans. Microw. Theory Tech.*, vol. MTT-17, no. 10, pp. 768–778, Oct. 1969.

[25] D. M. Pozar, "The active element pattern," *IEEE Trans. Antennas Propag.*, vol. 42, no. 8, pp. 1176–1178, Aug. 1994.

[26] W. L. Stutzman and G. A. Thiele, *Antenna Theory and Design*, 2nd ed. New York: Wiley, 1997.



Edwin Walter Reid received the B.Sc. degree in engineering physics and the Ph.D. degree from the University of Alberta, Edmonton, AB, Canada.

He is the President of Radio Frequency Works, which is a privately owned consulting engineering firm located at St. Albert, AB, Canada, that specializes in industrial/military applications of radio frequency (RF) energy. He has extensive experience in the design and modification of high-powered RF generators, transmission accessories, and antenna systems used in broadcasting, navigation, radar, and telecommunications.

Dr. Reid is registered as a Professional Engineer with the Association of Professional Engineers, Geologists, and Geophysicists of Alberta.



Laura Ortiz-Balbuena received the B.S. degree in electronics engineering from Universidad Autonoma Metropolitana and the Ph.D. degree in communications and electronics engineering from Instituto Politecnico Nacional.

She joined the Microelectronics Laboratory, Texas A&M University, Austin, in 1996 and was a Professor/Counselor for the IEEE students' branch for more than six years. She has gained the title Assessor of the Council on Accreditation of Engineering Education in Mexico, and she is one of the founders of the Masters in Microelectronics at the Instituto Politécnico Nacional (National Polytechnic Institute), Mexico City, Mexico. During her long career, she has been ranked as a top teacher and has been commended for being an excellent researcher. She joined the Microwave Laboratory, University of Alberta, Edmonton, AB, Canada, in September 2008, working in early breast cancer detection using microwaves. At present, she is working in 3-D image construction using radar information. She has been a Professor for more than 20 years and has published several papers in the areas of signal processing and microelectronics. She has acquired a patent for the architecture of the analog adaptive filter and was allowed by the New High Technology Development Foundation of Japan to build this architecture in integrated circuits.



Aliakbar Ghadiri (S'10) received the B.Sc. and M.Sc. degrees in electronics engineering from the Iran University of Science and Technology (IUST), Tehran, Iran, in 1998 and 2001, respectively. He is currently working toward the Ph.D. degree in electrical engineering at the University of Alberta, Edmonton, AB, Canada.

From 2000 to 2001, he was a Design Engineer with Kerman Tablo Co., Tehran, where he was working on the design of single- and three-phase digital power meters and testers. From 2002 to 2007, he was an Instructor at IUST, Behshahr, India. His research interests include the design of radio frequency (RF) building blocks for ultra-wideband and millimeter-wave applications. The focus area of his research is active-based implementation of passive devices for RF applications.



Kambiz Moez (S'01–M'07) received the B.Sc. degree in electrical engineering from the University of Tehran, Tehran, Iran, in 1999 and the M.A.Sc. and Ph.D. degrees from the University of Waterloo, Waterloo, ON, Canada, in 2001 and 2006, respectively.

Since January 2007, he has been an Assistant Professor with the Department of Electrical and Computer Engineering, University of Alberta, Edmonton, AB, Canada. His current research interests include the analysis and design of radio frequency CMOS integrated circuits and systems for a variety of applications, including wired/wireless communications, biomedical imaging, instrumentation, and automotive radars.